Application of lattice Boltzmann method to simulate microchannel flows

C. Y. Lim, C. Shu,[a] X. D. Niu, and Y. T. Chew
Department of Mechanical Engineering, National University of Singapore, 10 Kent Ridge Crescent, Singapore 119260

(Received 1 July 2001; accepted 17 April 2002; published 31 May 2002)

Microflow has become a popular field of interest due to the advent of microelectromechanical systems. In this work, the lattice Boltzmann method, a particle-based approach, is applied to simulate the two-dimensional isothermal pressure driven microchannel flow. Two boundary treatment schemes are incorporated to investigate their impacts to the entire flow field. We pay particular attention to the pressure and the slip velocity distributions along the channel in our simulation. We also look at the mass flow rate which is constant throughout the channel and the overall average velocity for the pressure-driven flow. In addition, we include a simulation of shear-driven flow in our results for verification. Our numerical results compare well with those obtained analytically and experimentally. From this study, we may conclude that the lattice Boltzmann method is an efficient approach for simulation of microflows. © *2002 American Institute of Physics.* [DOI: 10.1063/1.1483841]

I. INTRODUCTION

The existence of micromachining technology such as surface and bulk machining enables us to fabricate mechanical systems in micron size, which are generally referred as the microelectromechanical systems (MEMS). These systems, comprising mostly sensing and actuating components, are the integration of miniature mechanical devices and electronic circuits that have fast response time and are capable of achieving high spatial resolution due to their minute size—two attractive features from engineering application point of view. In addition, the fact that these devices are batch manufactured with techniques similar to silicon wafer fabrication makes MEMS very competitive from an economic point of view as well. The advent of these microsystems complements the development and understanding of new regimes in microflow by making experimental work possible, which in turn help calibrating MEMS and understanding their characteristics like a feedback loop. The main incentive to look at fluidic behavior at micron scale is that microdevices tend to behave much differently from the objects we are used to handling in daily life, requiring us to bring more factors into consideration. Under such circumstances, the inertial forces tend to be quite small, and the surface effects such as friction, electrostatic forces, and viscous effects tend to dominate their overall behavior as the surface to volume ratio becomes larger.

Minute dimensions have also extended these flow phenomena to higher degrees of rarefaction, which is often characterized by Knudsen number Kn, where Kn is the ratio of the mean free path λ to the characteristic length L. It is generally agreed that continuum fluid flow holds until $\mathrm{Kn}=0.01$, beyond which the continuum assumption breaks down in rarefaction due to sharp gradients of the flow parameters. The major concern in applying Navier–Stokes (NS) equations beyond this regime is that there may be simply too few molecules within a finite volume for continuum assumption to be valid. As Kn increases, the flow enters the "slip-flow" ($0.01<\mathrm{Kn}<0.1$) and "transition" ($0.1<\mathrm{Kn}<3$) regimes. In the slip-flow regime, the Navier–Stokes solver can still be used with introduction of a slip velocity at the solid boundary. In the transition regime, the rarefaction effect is critical, and the conventional flow solver, which is based on the computation of Navier–Stokes equations, is no longer applicable. In this case, a direct alternative would be particle-based methods. One of those efficient particle-based methods for simulation of microflows is the direct simulation of Monte Carlo (DSMC) method.[1] DSMC simulates molecular interactions of particles, which represents groups of molecules having the same properties such as velocity and temperature. Since a simulated particle representing a group of molecules having the same properties is taken as one independent variable, there is no need to consider each molecule individually among this specific group of molecules. The number of real molecules per simulated particle is called the scaling factor, which often ranges from 10^{10} to 10^{12} for a two-dimensional (2-D) problem. In actual DSMC computation, the gas is represented by many simulated particles distributed in cells in which all the macroscopic properties of the flow field are obtained by statistical analysis. The interparticle collision is carried out according to probability of collision, i.e., pairs of molecules are selected randomly for elastic collision within a cell or subcell. Since in the DSMC method, the number of particles distributed in the field is directly related to the number of molecules, the computational effort is usually very large.

Recently, another particle-based approach, the lattice Boltzmann method (LBM), has received considerable attention for simulation of viscous flows.[2–5] Unlike the DSMC method, the number of particles distributed in the field is not

[a]Author to whom all correspondence should be addressed; electronic mail: mpeshuc@nus.edu.sg

related to the number of molecules in the LBM. Instead, it is only dependent upon the number of mesh points and the lattice model. Therefore, it is much more computationally efficient than the DSMC method. For a typical case of Kn=0.05 and pressure ratio=2.5, LBM requires 92 s computational time and 1.86 Mbytes on a COMPAQ ALPHASERVER DS10, while DSMC requires 1.05×10^5 s and 5.08 Mbytes on the same machine. LBM only requires updating the density distribution functions, while DSMC requires tracing of 1.2×10^5 particles with position, velocities, as well as other auxiliary parameters.

Currently, the LBM is mainly applied to the continuum flow regime due to the availability of comparisons by conventional CFD solvers. As will be shown later, there is no continuum assumption involved in the LBM; therefore its prospective in simulating microflows is quite evident in principle. In this work, we will show that with proper implementation of boundary conditions, LBM is capable of simulating microflows. Our cases of study include 2-D pressure-driven and shear-driven microchannel flow at $0.010<\mathrm{Kn}<0.155$. The following shows that the LBM results are in good agreement with analytical solutions of Arkilic *et al.*[6] as well as experimental data.[7]

II. LATTICE BOLTZMANN METHOD

The origin of LBM can be traced back to the lattice-gas cellular automata[8] (LGCA), in which similar kinetic equation is shared

$$f_i(\mathbf{x}+\mathbf{c}_i\Delta t,t+\Delta t)=f_i(\mathbf{x},t)+\Omega_i(f_i(\mathbf{x},t)),\quad i=0,1,...,k, \tag{1}$$

where f_i is the Boolean algebra indicating the occupation state of particles in the i direction and k is the total number of lattice links; $\mathbf{c}_i$ is the particle velocity, the last term Ω_i in the equation represents the collision operator in accordance with arbitrary collision rules.

Recent lattice Boltzmann models are further simplified by replacing the Boolean algebra with a continuous distribution function[5] and also by linearizing the collision operator by Bhatnagar–Gross–Krook (BGK) approximation,[9,10] in which the nonlinear term Ω_i is expressed as the single time relaxation of f_i to local equilibrium,[11] yielding

$$f_i(\mathbf{x}+\mathbf{c}_i\Delta t,t+\Delta t)=f_i(\mathbf{x},t)-\frac{1}{\tau}[f_i(\mathbf{x},t)-f_i^{\mathrm{eq}}(\mathbf{x},t)],$$
$$i=0,1,...,k, \tag{2}$$

where f_i^{eq} is the local equilibrium distribution function, τ is the collision time. Note that the BGK approximation[11] is originally created for the Boltzmann equation, and for the continuum flow, τ is related to the viscosity. Alternatively, Eq. (2) can be derived from the discrete Boltzmann equation by using the upwind difference discretization. The Boltzmann equation with BGK approximation can be written as

$$\frac{\partial f(\mathbf{v},\mathbf{x},t)}{\partial t}+\mathbf{v}\cdot\nabla f(\mathbf{v},\mathbf{x},t)=-\frac{1}{\omega}[f(\mathbf{v},\mathbf{x},t)-f^{\mathrm{eq}}(\mathbf{v},\mathbf{x},t)], \tag{3}$$

where ω is called the relaxation time in the BGK collision model. It has been shown that the velocity space $\mathbf{v}$ can be discretized into a finite set of velocities $\{\mathbf{c}_i\}$ without affecting the conservation laws.[4] In the discrete velocity space, the Boltzmann equation becomes[12]

$$\frac{\partial f_i(\mathbf{x},t)}{\partial t}+\mathbf{c}_i\cdot\nabla f_i(\mathbf{x},t)=-\frac{1}{\omega}[f_i(\mathbf{x},t)-f_i^{\mathrm{eq}}(\mathbf{x},t)]. \tag{4}$$

Equation (4) is applied along the i velocity direction. The stream velocity can be taken as $\mathbf{c}_i=\Delta\mathbf{x}/\Delta t$. With this, application of upwind differencing to Eq. (4) gives[12]

$$f_i(\mathbf{x}+\mathbf{c}_i\Delta t,t+\Delta t)-f_i(\mathbf{x},t)=-\frac{\Delta t}{\omega}[f_i(\mathbf{x},t)-f_i^{\mathrm{eq}}(\mathbf{x},t)]. \tag{5}$$

Equation (5) is exactly the same as Eq. (2) if we set $\tau=\omega/\Delta t$. To apply Eq. (2) or Eq. (5), one has to determine the parameter τ or ω. For the continuum flow, we can perform Chapman–Enskog multiscale expansion to Eq. (2), and τ is determined in such a way that the Navier–Stokes equations are recovered. As a consequence, the parameter τ is given by

$$\nu=c_s^2\Delta t(\tau-0.5), \tag{6}$$

where ν is the kinematic viscosity and c_s is the speed of sound. However, for the microflow, the continuum assumption is not valid, and Eq. (6) is not applicable. For this case, τ should be related to the Knudsen number. Based on the BGK approximation, we assume that the collision happens and relaxes toward equilibrium within a distance of λ (mean free path of molecules) in duration ω when a particle travels a distance of Δx within a time interval of Δt. In other words, particles are assumed to travel a distance of λ while relaxing to their equilibrium state in a collision interval ω, which is also the relaxation time. The above-mentioned assumption can be mathematically put as

$$\bar{c}=\frac{\lambda}{\omega}\approx O\left(\frac{\Delta x}{\Delta t}\right), \tag{7}$$

where $\bar{c}$ is the mean speed of particle. In our simplified analysis, we choose $\lambda/\omega=\Delta x/\Delta t$ ($\Delta x=\Delta y$ due to square lattice). Finally, we obtain the following relationship:

$$\lambda=\tau\Delta x, \tag{8}$$

where τ is the dimensionless relaxation time seen in Eq. (2) or Eq. (5). Equation (8) will be used in the present work to simulate the microchannel flow. It is noted that in a recent work,[13] Nie *et al.* proposed another way to link τ with the local density. They also generated some accurate results for microflows.

In the present study, we employ a square lattice multispeed model, denoted by D2Q9[14] for its historical reasons as in the following:

$$c_0=(0,0),$$
$$c_i=\left(\cos\left(\frac{i-1}{4}\right)\pi,\sin\left(\frac{i-1}{4}\right)\pi\right)c,\quad i=1,...,8, \tag{9}$$

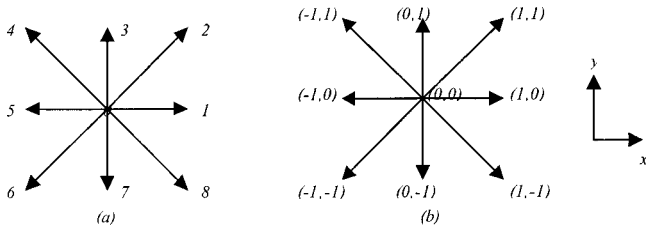

FIG. 1. A D2Q9 lattice model: (a) lattice directions; (b) lattice velocity vectors.

where c is the particle streaming speed. Multispeed models were developed to account for unphysical flow effects such as Galilean invariance[15] and explicitly pressure-velocity dependence as discussed by Chen *et al.*[16] In the early development of LGCA and LBM, lattice tensor isotropy had to be satisfied up to the fourth order in order to recover Navier–Stokes equations in the macroscopic incompressible limit. Generally, a ''reasonable'' lattice has to be invariant with respect to any arbitrary orthogonal transformations in the continuous space to avoid unphysical flow effects. This is the main reason to employ the multispeed square lattice in our LBM simulation. Other lattices of different shapes may be used as long as they do not bring along the above-mentioned problems, and their applications are straightforward. Figure 1 shows the square lattice employed in this work. The lattice vectors consist merely of unity components, which specify the propagation directions of particles after local collisions. When c is taken as 1, the lattice velocity $\mathbf{c}_i=(c_{ix},c_{iy})$ has unity magnitude for directions of $i=1$, 3, 5, and 7, and magnitude $\sqrt{2}$ for directions of $i=2$, 4, 6 and 8, as shown in Fig. 1.

When the distribution functions are computed, the macroscopic parameters can be easily determined from the following formulations:

$$\rho=\sum_{i=0}^{k} f_i, \quad \rho\mathbf{U}=\sum_{i=1}^{k} \mathbf{c}_i f_i, \quad P=\frac{1}{3}\rho c^2. \tag{10}$$

As such, the equilibrium distribution functions approximated from a Maxwellian distribution[14,17] can be defined as

$$f_0^{\mathrm{eq}}=\frac{4}{9}\rho\left[1-\frac{3}{2}\frac{\mathbf{U}^2}{c^2}\right], \tag{11}$$

$$f_i^{\mathrm{eq}}=\frac{1}{9}\rho\left[1+3\frac{\mathbf{c}_i\cdot\mathbf{U}}{c^2}+\frac{9}{2}\frac{(\mathbf{c}_i\cdot\mathbf{U})^2}{c^4}-\frac{3}{2}\frac{\mathbf{U}^2}{c^2}\right], \quad i=1,3,5, \text{ and } 7, \tag{12}$$

$$f_i^{\mathrm{eq}}=\frac{1}{36}\rho\left[1+3\frac{\mathbf{c}_i\cdot\mathbf{U}}{c^2}+\frac{9}{2}\frac{(\mathbf{c}_i\cdot\mathbf{U})^2}{c^4}-\frac{3}{2}\frac{\mathbf{U}^2}{c^2}\right], \quad i=2,4,6, \text{ and } 8. \tag{13}$$

In the traditional application, while recovering Navier–Stokes equations in macroscopic limit through a multiscale (Chapman–Enskog) expansion technique, the flow parameter such as the kinematic viscosity ν can be defined,[18] which will then be used in constructing the Reynolds number. As will be shown in Sec. III, we look into a different flow parameter, the Knudsen number, which will be used to determine the parameter τ in the application of LBM for the microflow.

III. MICROCHANNEL FLOW SIMULATION BY LATTICE BOLTZMANN METHOD

In this section, we will discuss how to apply the lattice Boltzmann method to simulate the microchannel flow. Special attention will be paid to the determination of τ from the given Knudsen number and the implementation of boundary conditions.

For the pressure-driven problem, the flow is driven by the pressure difference imposed at the inlet and outlet. With the given pressure ratio ($P_{\mathrm{inlet}}/P_{\mathrm{outlet}}$), the pressure values at the inlet and outlet are fixed during the computation. Accordingly, the density values at the inlet and outlet are determined at each time step. To start the computation, the desired Kn $=\lambda/H$ is first input, where H is the height of the channel. Since the square lattice is applied in the present work, H can be written as $H=(N_y-1)\Delta x$, where N_y is the number of mesh points in the y direction. So, from Eq. (8), τ can be computed as

$$\tau=\mathrm{Kn}(N_y-1). \tag{14}$$

With this formulation, it is quite impossible to have numerical simulation of Kn$=0$. However, this case (Kn$=0$) can be considered by conventional LBM, for instance, using Eq. (6). The local Knudsen number can be computed by

$$\mathrm{Kn}=\frac{\mathrm{Kn}_o}{P^*(X)}, \tag{15}$$

where X is the nondimensional x and the subscript o denotes outlet. τ will increase according to Eq. (14). As the reason for the increment of Kn along the channel is the decreasing pressure (density), the increase of τ which is related to the mean free path in the lattice context is well justified, looking at the fact that the mean free path is inversely proportional to the density. Having defined Kn, appropriate N_y and τ could be selected, which would then be used in the determination of mesh size and the collision-propagation updating procedure, respectively. For the case of Kn$=0.05$, the number of nodes across the channel is $N_y=21$ and τ is taken as 1 at the outlet, while the length to height ratio has been kept at 10 throughout. For helium at Kn$=0.05$, the corresponding height of the channel is equal to 4.123 μm and the length of the channel is 41.23 μm. As mentioned earlier, τ varies along the channel according to Eq. (14). For the case of Kn$=0.1$, the channel height is 10 lattice units with the length to height ratio kept at 10. Note that the degree of rarefaction is affected by two factors, namely the mean free path and the characteristic length. Although there is no proof in equating the same degree of rarefaction by low density (large λ) and by minute geometries (small L), we treat the dimensionless number Kn as general, irrespective of its origin. With this approach, there is literally no restriction on the flow regime from the point of governing equations, as encountered by its

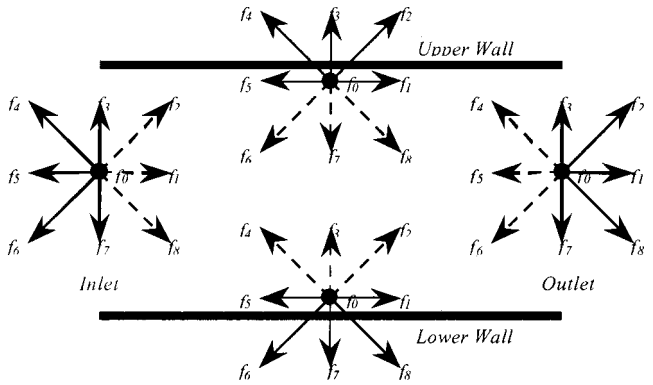

FIG. 2. Configuration of distribution functions at boundary points: solid lines represent known functions while dashed lines represent unknown functions.

NS solvers counterpart, in which rarefaction breaks down the continuum of flow and causes the NS approach to be invalid at high Kn.

With τ value, Eq. (2) can be applied at all interior points for all the lattice directions. However, at the boundary points, the distribution functions along some lattice directions (outward) can be computed from Eq. (2) while some others have to be given from the boundary condition. The lattice directions of D2Q9 at the inlet, outlet, and the solid walls are shown in Fig. 2, where the solid lines represent known distribution functions streamed from the flow domain while dashed lines are unknown functions to be determined by the boundary treatments. Clearly, at the inlet, five distribution functions f_3, f_4, f_5, f_6, and f_7 can be computed from Eq. (2), and three distribution functions f_1, f_2, and f_8 are to be specified. Similarly, at the outlet, f_1, f_2, f_3, f_7, and f_8 can be computed from Eq. (2); but f_4, f_5, and f_6 have to be given from the boundary condition. In this work, we use equilibrium distribution functions to update the unknown functions at the inlet and outlet, respectively. Note that in the equilibrium distribution function, the density and velocity components u and v have to be given. In our work, the density values at the inlet and outlet are fixed, and u and v are extrapolated from the flow domain. So, the three unknown functions at the inlet and outlet are given by

$$\left.\begin{aligned} f_1(0,y,t) &= f_1^{\mathrm{eq}}(\rho,u,v,0,y,t)\\ f_2(0,y,t) &= f_2^{\mathrm{eq}}(\rho,u,v,0,y,t)\\ f_8(0,y,t) &= f_8^{\mathrm{eq}}(\rho,u,v,0,y,t)\end{aligned}\right\} \quad \text{at inlet,} \tag{16}$$

$$\left.\begin{aligned} f_5(L,y,t) &= f_5^{\mathrm{eq}}(\rho,u,v,L,y,t)\\ f_4(L,y,t) &= f_4^{\mathrm{eq}}(\rho,u,v,L,y,t)\\ f_6(L,y,t) &= f_6^{\mathrm{eq}}(\rho,u,v,L,y,t)\end{aligned}\right\} \quad \text{at outlet,} \tag{17}$$

where L is the length of the channel. Figure 2 also shows that on the solid boundaries (top and bottom boundaries), five distribution functions can be computed from Eq. (2) while another three functions must be determined by the boundary condition. The existence of slip velocity on the solid wall makes the implementation of boundary condition on the solid wall critical for the microflow simulation. In this work, we adopt two methods to study the effects of boundary conditions on the solid wall. The first one is the specular boundary condition. As shown in Fig. 2, this boundary condition gives

$$\left.\begin{aligned} f_2(x,0,t) &= f_8(x,0,t)\\ f_3(x,0,t) &= f_7(x,0,t)\\ f_4(x,0,t) &= f_6(x,0,t)\end{aligned}\right\} \quad \text{at lower wall,} \tag{18}$$

$$\left.\begin{aligned} f_8(x,H,t) &= f_2(x,H,t)\\ f_7(x,H,t) &= f_3(x,H,t)\\ f_6(x,H,t) &= f_4(x,H,t)\end{aligned}\right\} \quad \text{at upper wall.} \tag{19}$$

Equations (18) and (19) are analogous to a reflection of a particle hitting a wall specularly, taking the distribution function as a representation of a group of particles having the same velocity approaching the wall. Earlier bounce back condition[19] was used heuristically to ensure no slip condition while this specular condition enables us to capture the slip at the wall. As far as the LGCA and LBM are concerned, this heuristic boundary condition is popular and is a heritage from their successor models. We used specular bounce back for its simplicity and historical reasons. More important, this is the most direct and simple method to yield slip at wall. At this point, some attention should be drawn to the specular slip having 0 accommodation factor in Maxwellian slip, which is unphysical. As shown, our specular model in LBM still has some momentum ''deposited'' on the wall, only the unknown density distribution functions are defined by their corresponding specular directions, with other functions being propagated from interior lattice nodes. In other words, ''specular'' is loosely used in our boundary definition due to its historical as well as particle–wall interaction in lattice context. There is no other relationship other than the conceptual idea of ''elastic reflection'' of particles in defining the unknown by the known functions. Looking at only limited speeds and restricted lattice directions, the specular approach remains the feasible and practical ''averaging'' means in resolving this issue.

Another kind of boundary treatment on the wall is an extrapolation scheme, which approximates the density and stream velocity u at solid boundaries (the normal velocity v is always set to zero) by a second-order polynomial extrapolation form. The unknown distribution functions at wall are then approximated by their equilibrium functions. This approximation may be justified by the fact that all distribution functions eventually converge to their equilibrium states. The main objective here is to investigate the direct effects of boundary treatments used in the lattice boundaries on the entire flow properties, and more important, their contributions to slip velocities. In this extrapolation scheme, no heuristic assumption is inherited, but it assumes that the fluid properties are continuous from the interior flow field to the solid boundary.

Since Eq. (2) mainly describes the kinetics of particles in the simulated flow, i.e., local collision and propagation, it can be split into two numerical steps accordingly:

$$f_i^*(\mathbf{x},t) = f_i(\mathbf{x},t) - \frac{1}{\tau}[f_i(\mathbf{x},t) - f_i^{\mathrm{eq}}(\mathbf{x},t)], \tag{20}$$

$$f_i(\mathbf{x}+c_i\Delta t, t+\Delta t)=f_i^*(\mathbf{x},t). \tag{21}$$

Upon calculating all f_i^{eq} which are only functions of the macroscopic parameters (namely ρ, u, and v) in the flow domain, local collisions will be performed [Eq. (20)], which are followed by global propagations [Eq. (21)]. Those distribution functions at boundaries that cannot be determined by propagation procedure are exceptional to this algorithm and will be attained according to our boundary treatments mentioned earlier.

IV. RESULTS AND DISCUSSION

Beskok *et al.*[20] indicated that there are four major effects occurred in microflow, namely rarefaction, compressibility, thermal creeping, and viscous heating. The first two effects will be more relevant in the present isothermal analyses, which can be shown by our pressure and velocity profiles. We are particularly interested in the slip flow regime ($0.01<\mathrm{Kn}<0.1$) where the flow is still deemed valid when solved using Navier–Stokes equations with slip boundary condition. Four cases were simulated, i.e., 2-D microchannel flow with $\mathrm{Kn}=0.05$ and 0.1 and with two boundary treatments mentioned earlier, i.e., specular reflection (Spec) and the extrapolation method (U Ext). Arkilic *et al.*[6] obtained analytical Navier–Stokes solution at low Kn with a first-order slip model for 2-D microchannel flow, in which the general pressure and velocity profiles were described. As predicted by Arkilic *et al.*,[6] the pressure distribution can be given as

$$P^*=-6\sigma\,\mathrm{Kn}+\sqrt{(-6\sigma\,\mathrm{Kn})^2+(1+12\sigma\,\mathrm{Kn})X+(\mathrm{Pr}^2+12\sigma\,\mathrm{Kn}\,\mathrm{Pr})(1-X)}, \tag{22}$$

where σ is the accommodation factor which is effectively 1 for most engineering cases, Pr is the pressure ratio of inlet to outlet. The gas–wall accommodation coefficient varies with surfaces and is specified before numerical simulation by NS solvers, and it is often obtained via experiments (or numerical experiments), which varies with different solid–gas interfaces. In our numerical simulation, there is no need to specify this accommodation factor, as required in the conventional Navier–Stokes solution. The specular approach allows us to specify the boundary condition through tracing particles' reflection intrinsically, just like other particle-based methods such as DSMC. In Figs. 3–5, our numerical results yield the same profiles as given by Arkilic *et al.*, and these profiles remain similar in general in our numerical simulations.

In this section, the negation of nonlinearity in pressure distribution (compressibility) as Kn increases is discussed, and experimental results from UCLA[7] are also benchmarked to examine our numerical results in transition flow regime ($0.1<\mathrm{Kn}<3$). In spite of the differences in modeling approaches, both Arkilic and present results are expected to be comparatively similar since both of them fall within the same slip-flow regime, as illustrated in Figs. 6–12.

Figure 3 shows the pressure distribution in the channel, where the pressure P^* has been normalized by the outlet pressure, and the x coordinate is normalized by the channel length. (*) Here an asterisk denotes the nondimensionalization of a flow variable. It can be shown that P^* is only dependent on X, and that it remains unchanged across the channel. Figures 4 and 5 illustrate the u and v velocities, respectively. In general, Fig. 4 exhibits the general characteristics of microchannel flow, in which the slip and centerline velocities increase along the channel due to decreasing pres-

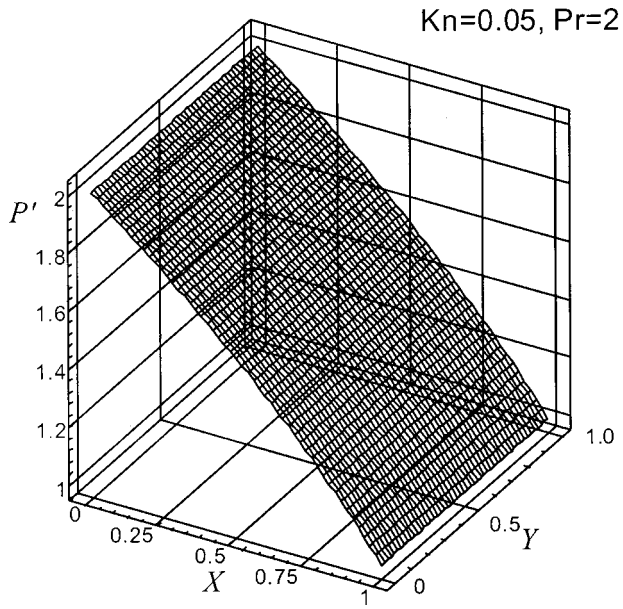

FIG. 3. Normalized pressure distributions predicted by the specular scheme at $\mathrm{Pr}=2.00$, $\mathrm{Kn}=0.05$.

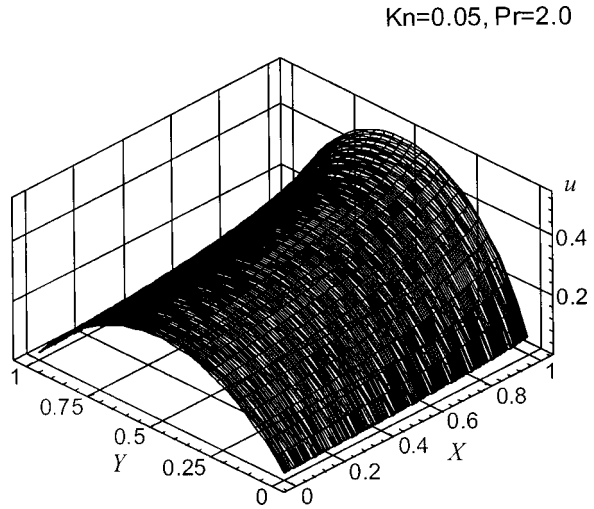

FIG. 4. u-velocity profile predicted by the specular scheme at $\mathrm{Pr}=2.00$, $\mathrm{Kn}=0.05$.

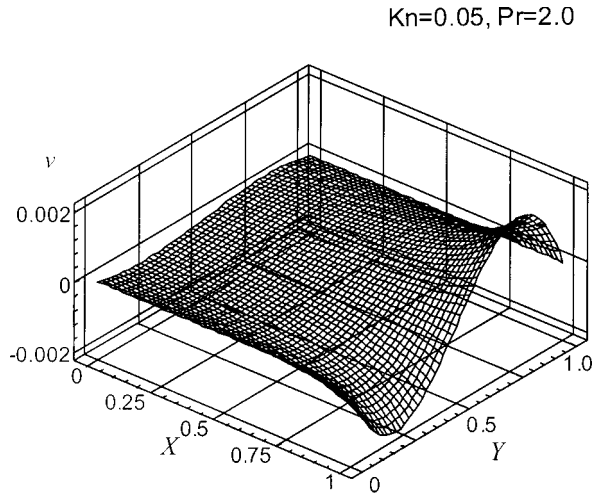

FIG. 5. v-velocity profile predicted by the specular scheme at Pr=2.00, Kn=0.05.

sure, and that the parabolic velocity profile across the channel is symmetrical throughout. Figure 5 confirms the v profile obtained by Arkilic *et al.*,[6] in which the velocity is zero at the centerline and solid boundaries, and that the maximum points are opposite to each other and skewed toward the walls. However, its relative importance is not as significant as P^* and u, because its magnitude is of several orders smaller. Nonetheless, this characteristic of flow captured by the present approach confirms the existence of lateral velocity v as shown in the analytical solution.

In Fig. 6, we compare the nonlinearity of pressure ($P' = P_x^* - P_{\text{linear}}^*$) obtained by various methods mentioned earlier at Pr=2.0 within slip-flow regime, at Kn=0.05 and Kn=0.10, respectively. Similar to that predicted by the analytical solutions, both boundary treatment schemes are able to show the negation of nonlinearity in pressure ($P' = P_x^* - P_{\text{linear}}^*$) as rarefaction increases. This nonlinearity in pressure distribution is a consequence of the compressibility effect in microflow according to Beskok *et al.* Figures 7 and 8 on the other hand illustrate P' for a spectrum of pressure

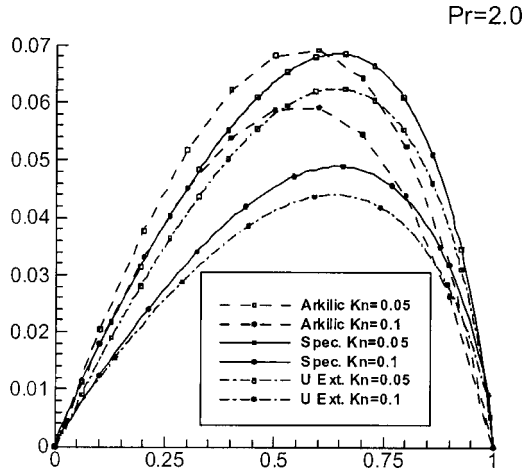

FIG. 6. Comparison of nonlinearity of pressure P' obtained by specular (Spec) and extrapolation (U Ext.) schemes with analytical solution at Pr=2.0, Kn=0.05, and 0.1.

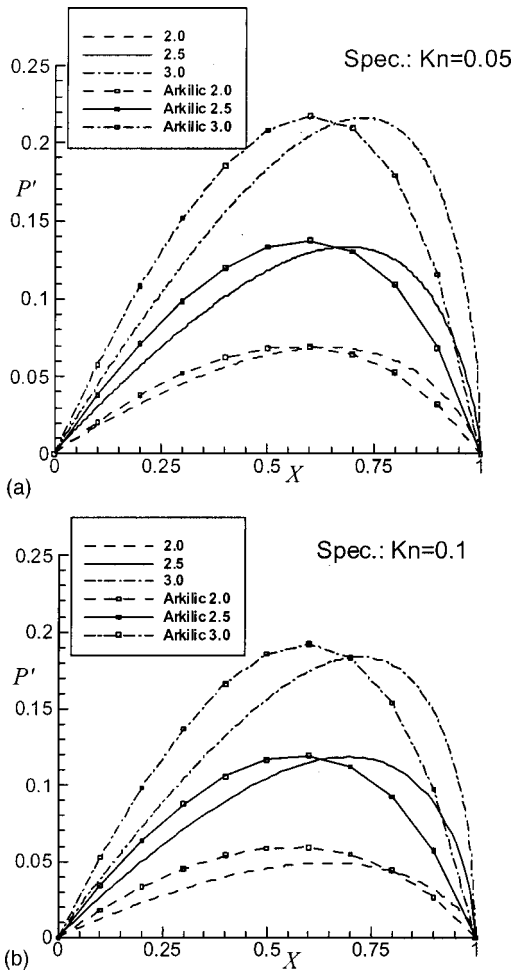

FIG. 7. Comparison of nonlinearity of pressure P' obtained by the specular (Spec) scheme with analytical solution at different pressure ratios for (a) Kn=0.05, and (b) Kn=0.1.

ratios ranging $2.0 < \text{Pr} < 3.0$ obtained using different boundary treatment schemes. The compressibility effect is enhanced by larger pressure ratios in both cases, and there is also a consistent deficit in magnitude between our numerical results and Arkilic's, which are more obviously illustrated in Figs. 9 and 10. The deviation may be due to the fact that the rarefaction effect is only accounted for in Arkilic's solution by incorporating a first-order slip while we look at the issue in a more rarefied sense where the molecular dimensions are concerned. In concluding this remark, we compare our results and Arkilic's results to the experimental results of UCLA,[7] as shown in Figs. 9 and 10. Arkilic's results overpredict P' in both cases, and the overprediction becomes more obvious at larger Kn. Our results show that the nonlinearity in pressure which is the reverse indicator of rarefaction does not vary much for both boundary schemes. This suggests that the boundary treatment mechanism has little influence on the pressure distribution. Another interesting point is that the peak of nonlinearity is skewed toward the outlet; this phenomenon is clearly exhibited by both Arkilic's and the present results. However, we report a more severe skewness, in which the peak occurs at $0.6 < X < 0.7$, compared to almost consistently at roughly 0.6 in Arkilic's results. It is also

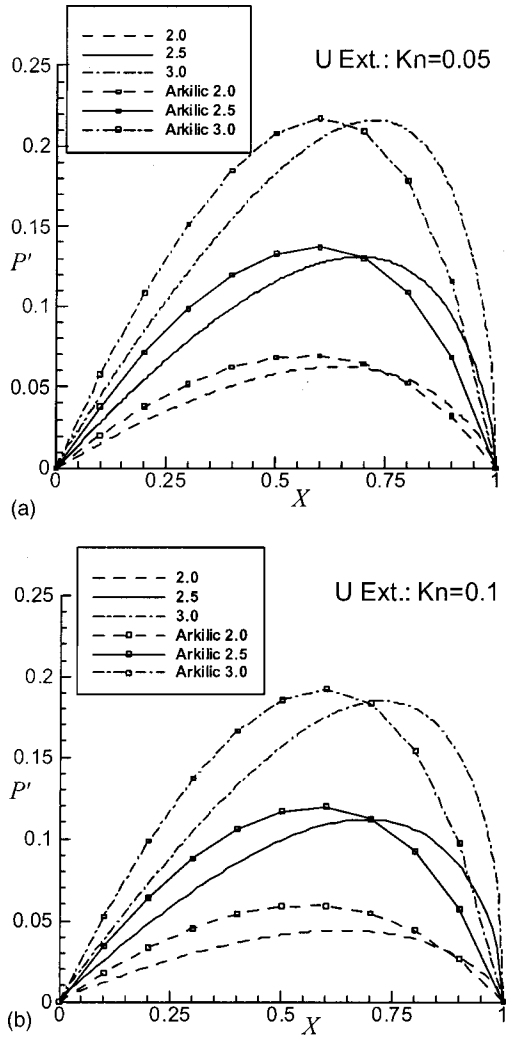

FIG. 8. Comparison of nonlinearity of pressure P' obtained by the extrapolation (U ext) scheme with analytical solution at different pressure ratios for (a) Kn$=0.05$, and (b) Kn$=0.1$.

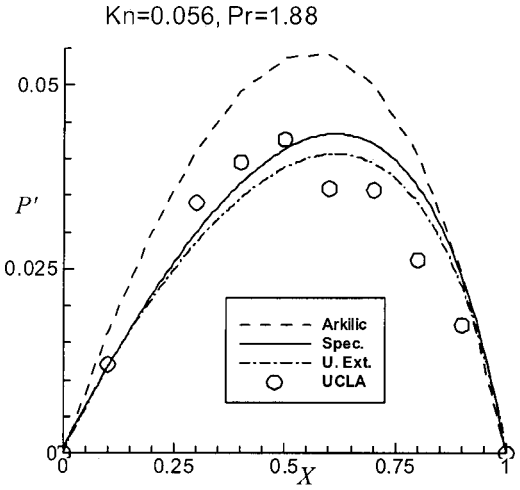

FIG. 9. Comparison of nonlinearity of pressure P' between present results, Arkilic's analytical results, and experimental data at Pr$=1.88$, and Kn $=0.056$.

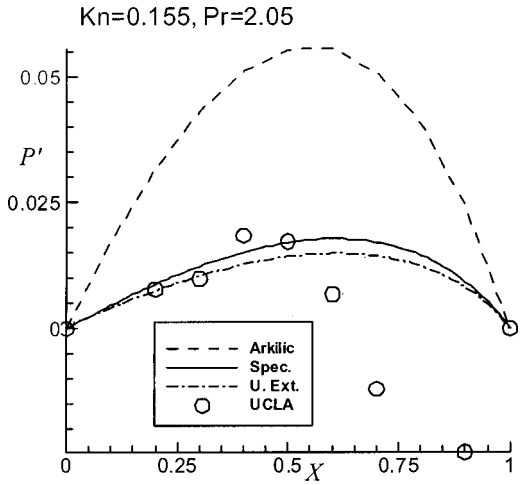

FIG. 10. Comparison of nonlinearity of pressure P' between present results, Arkilic's analytical results, and experimental data at Pr$=2.05$, and Kn $=0.155$.

shown that larger pressure ratio will further delay the peak to the outlet and that Kn has little effect on its location.

Figures 11 and 12 show the slip velocities along the channel that are normalized to the outlet centerline velocity

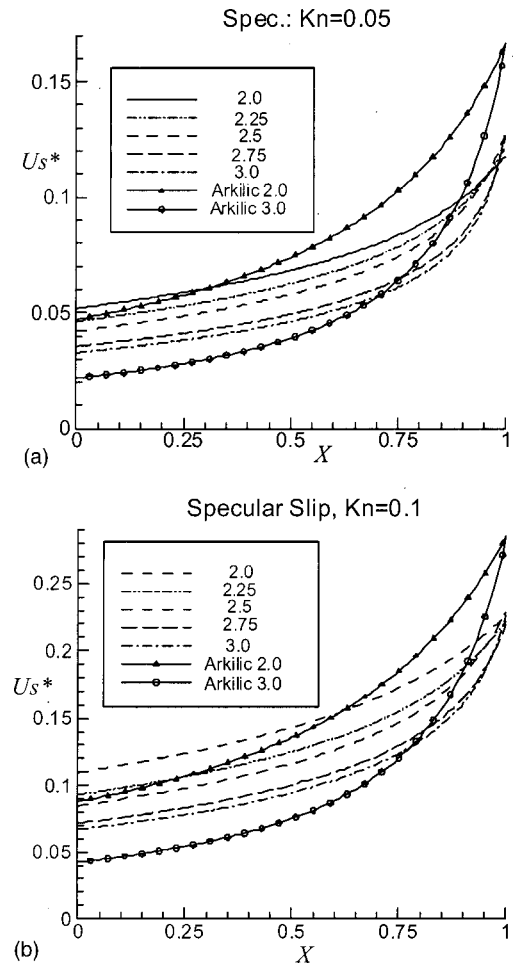

FIG. 11. Comparison of slip velocity at wall between present results obtained by the specular (Spec) scheme and Arkilic's analytical results at different pressure ratios for (a) Kn$=0.05$, and (b) Kn$=0.1$.

predicted by the specular and extrapolation schemes, respectively. Both present results predict smaller slip at wall toward the outlet, with the specular model [Figs. 11(a) and 11(b)] comparatively well fitted in the capsule of analytical predictions. Both models exhibit better resemblance at higher Kn, as depicted in Figs. 11(b) and 12(b). There are two features that are commonly shared: the decreasing trend for slip velocity at pressure rise and the convergence of a unique value of slip at outlet for various Pr's. According to Arkilic *et al.*, the slip at wall u_s^* at outlet is only dependent on Kn, given by

$$u_{s,o}^* = 1 - \frac{1}{1+4\sigma\,\mathrm{Kn}_o}, \tag{23}$$

where σ is a parameter (accommodation factor) in Arkilic's solution and is set to 1, and Kn_o is the outlet Knudsen number. Since local Knudsen number is a function of density that varies along the channel, the outlet Knudsen number which is usually at atmospheric conditions and constant is used in representing the flow for general cases. In present work, we keep up this consistency and characterize every simulation case by their outlet Knudsen numbers. In general, slip at wall can be expressed in terms of outlet slip $u_{s,o}^*$ that is function of Kn, Pr, and $\partial P^*/\partial X|_x$, shown in the following:

$$u_s^* = \frac{\Theta}{\mathrm{Pr}} U_{s,o}^* = \Psi u_{s,o}^*, \tag{24}$$

where Θ denotes the ratio of local to outlet pressure gradient and the subscripts x and o denote location along the channel and the outlet position, respectively. Θ and $\partial P^*/\partial X|_x$ can be written as

$$\Theta = \frac{\partial P^*/\partial X|_x}{\partial P^*/\partial X|_o}, \tag{25}$$

$$\left.\frac{\partial P^*}{\partial X}\right|_x = \frac{1+12\sigma\,\mathrm{Kn}-(\mathrm{Pr}^2+12\sigma\,\mathrm{Kn\,Pr})}{2\sqrt{(6\sigma\,\mathrm{Kn})^2+(1+12\sigma\,\mathrm{Kn})X+(P^2+12\sigma\,\mathrm{Kn\,Pr})(1-X)}}. \tag{26}$$

Parameter Ψ is inversely proportional to Pr; this explains Figs. 11 and 12 about the reduction of normalized inlet slip velocities. In general, slip velocity grows with Pr, but since the normalizing parameter $U_{\max}$ grows more effectively than u_s, we observe a decline in slip as Pr increases. Both of our boundary treatment schemes predict the outlet slip (Pr invariant) to be generally lower than that by NS first-order slip model. The reasoning of this may be that mere first-order slip incorporation in NS equations does not sufficiently and accurately account for the slip phenomenon. They require explicit supplements such as the continuum assumptions and accommodation factor σ. Shrinking grid size will not be effective and the only way to account for it is to have a slip fluid–wall interaction, which often requires a Maxwellian first-order slip with predetermined accommodation factor σ. LBM, which solves the discrete Boltzmann equation, does not require continuum assumption nor does it require explicit supplementary knowledge such as σ. Hence, we consider it more general for microflow simulations. Navier–Stokes equations, being one of the particular solutions of the Boltzmann equation by the Chapman–Enskog method, are generally used for the slip-flow regime only where the microeffects are not profound, as discussed previously.

Figures 11 and 12 also reveal that, as Kn increases, the slip velocity increases. This well reflects the physical phenomenon. As we know, in the continuum flow regime (Kn is very small), there is no slip velocity (zero value). When the flow enters the slip-flow regime, the slip velocity occurs. In other words, the slip velocity should physically increase with increase of Kn. Our results confirms this phenomenon. The slip velocities are quite different as shown in our numerical results; this implies that the choice of boundary treatment is sensitive for slip velocity but not the pressure distribution. Due to the nature of these boundary treatments, slip at wall is predicted differently, the specular model allows more slip at wall while the extrapolation scheme is more conservative at $\mathrm{Kn}=0.05$. To further investigate the sensitivity of these boundary schemes, we study the mass flow rate contributed by both schemes and our numerical predictions reveal that the difference of both boundary schemes is quite insignificant on average.

A more meaningful parameter to look at is the mass flow rate per unit width, which can be computed by $\dot{m}^*/w = \Sigma\,\rho^* u^* \Delta y$. Our numerical results show a constant mass flow rate throughout the channel, which should be the case. For this reason, the mass flow rate is calculated at $X=1$, using the above-mentioned formula. Dimensionalizing it by the outlet density, reference speed which is the average outlet speed, and the mean free path of helium at atmospheric condition (206 nm), it is then compared to the expression fitted for Arkilic's data (using current channel dimensions) in Figs. 13(a) and 13(b).

Finally, since the mass flow rate—which can be thought of as a product of density, average velocity, and cross-sectional area—is constant along the channel, we can obtain an overall average velocity for a specific Kn and Pr by a further division of the channel height. We then plot the averaged velocity $\Sigma u^* \Delta y/H$ predicted by Spec and U Ext schemes against the Knudsen number ranging from 0.04 and 0.1 at $X=1$ in Fig. 14. Arkilic's nondimensionalized average velocity at the outlet is also shown in Fig. 14. Both our numerical results and Arkilic's expression show the decreasing trend of average velocity when Kn increases. A curve is fitted to define the trend numerically, which gives

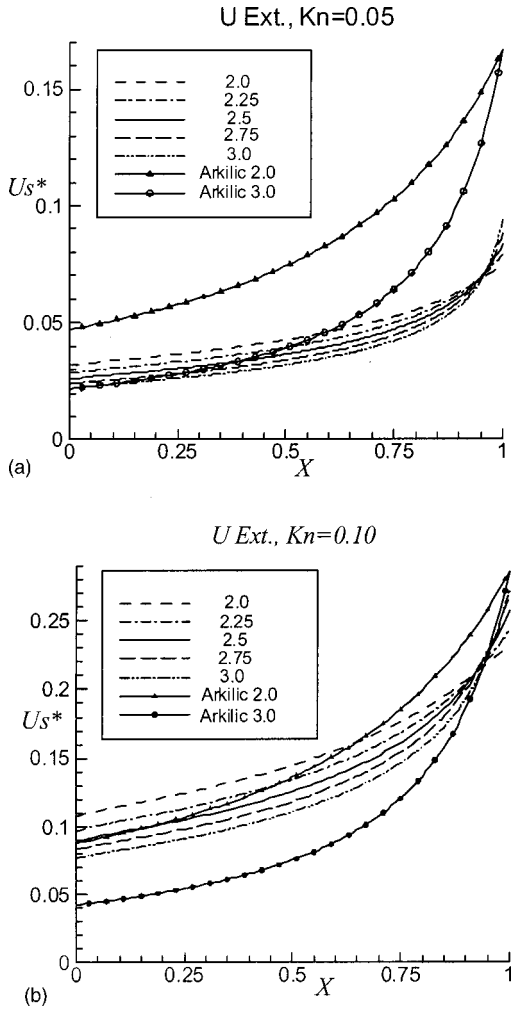

FIG. 12. Comparison of slip velocity at wall between present results obtained by the extrapolation (U ext) scheme and Arkilic's analytical results at different pressure ratios for (a) Kn=0.05, and (b) Kn=0.1.

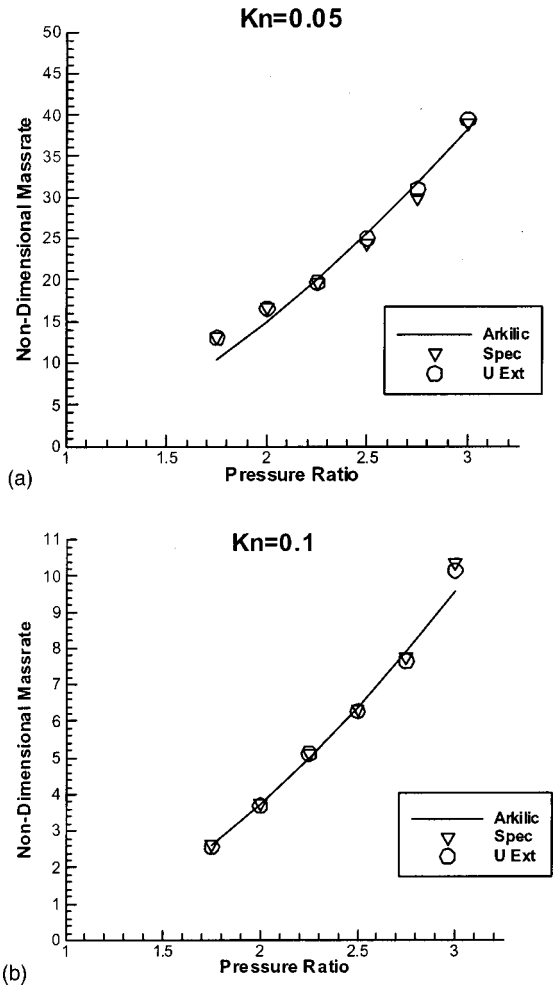

FIG. 13. Comparison of mass flow rates predicted by current boundary schemes with analytical expression by Arkilic *et al.* at different pressure ratios for (a) Kn=0.05, and (b) Kn=0.1.

$$u^* = \frac{0.5767}{\mathrm{Kn}} - 3.6357. \tag{27}$$

We also include a shear-driven 2-D microchannel flow at Kn=0.01 for verification. In Fig. 15, the *u* velocity profile is normalized using the shearing velocity at the upper moving wall. The boundary treatment at solid boundary is our specular model, and for the open boundary, periodic boundary condition is employed. Also included in Fig. 15 are the analytic solution and DSMC results. Since there will be no density change in isothermal cases,[1,21] the velocity profile is solely dependent on the shearing motion of the upper moving plate, and is a linear distribution across the channel if Navier–Stokes equation is solved ($d^2u/dy^2=0$) with equal Maxwellian slip

$$u_s = \frac{2-\sigma}{\sigma}\mathrm{Kn}\left.\frac{\partial u}{\partial y}\right|_w$$

at both walls. The velocity profile can be expressed as

$$u^* = \frac{1}{1+2\sigma\,\mathrm{Kn}}(y+\mathrm{Kn}), \tag{28}$$

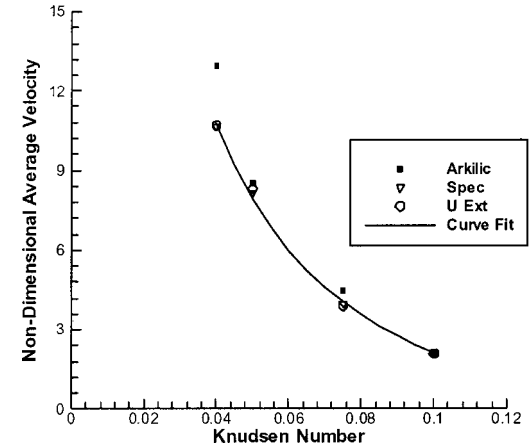

FIG. 14. Nondimensionalized average velocity at outlet by current boundary schemes with analytical expression by Arkilic *et al.* at different pressure ratios for (a) Kn=0.05, and (b) Kn=0.1.

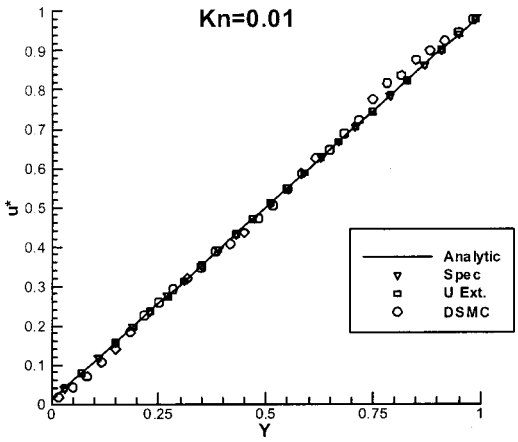

FIG. 15. Comparison of velocity profiles across the channel by different schemes for shear-driven flow at Kn=0.01.

where σ taken as 1 best fits the results. As shown, LBM's prediction shows excellent comparison to the analytic solution while the DSMC's results scatter around the line.

V. CONCLUSIONS

The particle-based lattice Boltzmann method (LBM) is successfully applied in this work to simulate a two-dimensional microchannel flow driven by a pressure difference and a shearing motion. Two approaches are presented to implement the boundary condition on the solid wall. For pressure-driven cases, particular attention is paid to the nonlinear pressure distribution and the slip-velocity distribution along the channel. Other important parameters such as mass flow rate and average velocity are also studied. The pressure distributions obtained by the present method compares well with the experimental data as well as Arkilic's analytical solution. In fact, the present results are closer to the experimental data than Arkilic's results, especially in the transition flow regime. Our numerical results confirm the rarefaction's negation on nonlinearity of pressure. The slip predicted by both boundary treatment schemes fall in the spectrum of that predicted by Arlilic's analytical method, particularly at higher Kn in the slip-flow regime. Our results confirm that the normalized slip diminishes with Pr, and the normalized outlet slip is only dependent on Kn. Both boundary schemes are also verified by a shear driven case at Kn=0.01, in which both exhibit the same prediction as expressed by analytic solution.

In short, both the specular model and extrapolation schemes capture slip at wall, by different methodology and principles. Since heuristic boundary conditions (specular model) is a well-accepted methodology in LGCA and LBM, it is our tendency to support it if asked to choose between these two, looking at the extrapolation scheme's pure mathematical premise. However, the extrapolation scheme gives us an alternative to obtain slip and other properties at solid boundaries other than the heuristic model, which is done by considering the internal flow field in estimating properties at walls.

[1] G. A. Bird, *Molecular Gas Dynamics and the Direct Simulation of Gas Flows* (Oxford University Press, New York, 1994).
[2] F. J. Higuera and J. Jimenez, "Boltzmann approach to lattice gas simulations," Europhys. Lett. **9**, 663 (1989).
[3] T. Abe, "Derivation of the lattice Boltzmann method by means of the discrete ordinate method for the Boltzmann equation," J. Comput. Phys. **131**, 241 (1997).
[4] X. He and L.-S. Luo, "*A priori* derivation of the lattice Boltzmann equation," Phys. Rev. E **55**, 6333 (1997).
[5] G. R. McNamara and G. Zanetti, "Use of the Boltzmann equation to simulate lattice-gas Automata," Phys. Rev. Lett. **61**, 2332 (1988).
[6] E. B. Arkilic, M. A. Schmidt, and K. S. Breuer, "Gaseous slip flow in long microchannels," J. Microelectromech. Syst. **6**, 167 (1997).
[7] K.-C. Pong, C.-M. Ho, J. Liu, and Y.-C. Tai, "Non-linear pressure distribution in uniform microchannels," Application of Microfabrication to Fluid Mechanics, ASME Winter Annual Meeting, Vol. **197**, 1994, p. 51.
[8] U. Frisch, B. Hasslacher, and Y. Pomeau, "Lattice-gas automata for the Navier–Stokes equation," Phys. Rev. Lett. **56**, 1505 (1986).
[9] S. Chen, H. D. Chen, D. Martinez, and W. H. Matthaeus, "Lattice Boltzmann model for simulation of magnetohydrodynamics," Phys. Rev. Lett. **67**, 3776 (1991).
[10] Y. H. Qian, Ph.D. thesis, Université Pierre et Marie Cure, Paris, 1990.
[11] P. L. Bhatnagar, E. P. Gross, and M. Krook, "A model for collision processes in gases. I. Small amplitude processes in charged and neutral one-component systems," Phys. Rev. **94**, 511 (1954).
[12] D. A. Wolf-Gladrow, *Lattice-gas Cellular Automata and Lattice Boltzmann Models: An Introduction*, Lecture Notes in Mathematics, Vol. 1725 (Springer, Berlin, 2000).
[13] X. Nie, G. D. Doolen, and S. Y. Chen, "Lattice Boltzmann simulation of fluid flows in MEMS," J. Stat. Phys. **107**, 279 (2002).
[14] Y. H. Qian, D. d'Humières, and P. Lallemand, "Lattice BGK models for Navier–Stokes equation," Europhys. Lett. **17**, 479 (1992).
[15] A. K. Gunstensen and D. H. Rothman, "A Galilean-invariant immiscible lattice gas," Physica D **47**, 53 (1991).
[16] Y. Chen, M. Lee, K. H. Zhao, and G. D. Doolen, "A lattice gas model with temperature," Physica D **37**, 42 (1989).
[17] H. Chen, S. Chen, and W. H. Matthaeus, "Recovery of the Navier–Stokes equations using a lattice-gas Boltzmann method," Phys. Rev. A **45**, R5339 (1992).
[18] X. He, Q. Zou, L.-S. Luo, and M. Dembo, "Analytic solutions of simple flows and analysis of nonslip boundary conditions for the lattice Boltzmann BGK model," J. Stat. Phys. **87**, 115 (1997).
[19] D. P. Ziegler, "Boundary conditions for lattice Boltzmann simulations," J. Stat. Phys. **71**, 1171 (1993).
[20] A. Beskok, G. E. Karniadakis, and W. Trimmer, "Rarefaction and compressibility effects in gas microflows," J. Fluids Eng. **118**, 448 (1996).
[21] L. S. Pan, G. R. Liu, and K. Y. Lam, "Determination of slip coefficient for rarefied gas flows using direct simulation Monte Carlo," J. Micromech. Microeng. **9**, 89 (1999).